Bioconjugate Synthesis of NiFe2O4 Using Juglans Regia Leaves Extract: Phytochemical Analysis, Optical Activity, Removal of Ciprofloxacin and Congo Red From Water

Muhammad TAJ (dr.taj@iub.edu.pk)
Islamia University of Bahawalpur
Muneera Alkahtani
Princess Nourah bint Abdulrahman University
Ahmad Raheel
Quaid-i-Azam University
Saima Shabbir
Institute of Space Technology
Rida Fatima
Quaid-i-Azam University
Sadia Aroob
Islamia University of Bahawalpur
Sadia Noor
University of Agriculture Faisalabad
Raja Ahmad
National Centre for Physics Islamabad
Heba Alshater
Elmenoufia university egypt

Research Article

Keywords: Bio template, Spinel ferrite, Optical activity, Degradation, Ciprofloxacin, Congo red

Posted Date: November 25th, 2020

DOI: https://doi.org/10.21203/rs.3.rs-109392/v1

Version of Record: A version of this preprint was published at Scientific Reports on March 8th, 2021. See the published version at https://doi.org/10.1038/s41598-021-84983-3.

Bioconjugate synthesis of $NiFe_2O_4$ using *Juglans regia* leaves extract: Phytochemical analysis, optical activity, removal of ciprofloxacin and Congo red from water

Muhammad Babar Taj[a]*, Muneera D. F. Alkahtani[b]*, Ahmad Raheel[c], Saima Shabbir[d], Rida Fatima[e], Sadia Aroob[a], Sadia Noor[f], Raja Hammad Ahmad[g]*, Heba Alshater[h]

[a]*Department of Chemistry, Islamia University Bahawalpur, Bahawalpur 63100 Pakistan*

[b]*Department of Biology, College of Science, Princess Nourah Bint Abdulrahman University, Riyadh 11657, Saudi Arabia*

[c]*Department of Chemistry, Quaid-e-Azam University, Islamabad 44000, Pakistan*

[d]*Department of Materials Science and Engineering, Institute of Space Technology, Islamabad 44000, Pakistan*

[e]*Department of Plant Sciences, Quaid-e-Azam University, Islamabad 44000, Pakistan*

[f]*Department of Chemistry, University of Agriculture, Faisalabad 38000 Pakistan*

[g]*Department of Nano Science and Technology, National Centre for Physics Islamabad 44000, Pakistan*

[h]*Department of Forensic Medicine and Clinical Toxicology, Elmenoufia University, Al Minufya, 32511, Egypt*

*Shared Correspondence: Muhammad Babar Taj (M. B. Taj), dr.taj@iub.edu.pk; mdf.alkahtani@gmail.com, Raja Hammad Ahmad, rhahmadatncp@gmail.com

Abstract

In recent years, the biogenic synthesis of nanoparticle received enormous attention due to simple and eco-friendly path. Here in Jr.$NiFe_2O_4$ nanoparticles (NPs) were synthesized first time using the leave extract of *Juglans regia* via a straightforward process. The physio and phytochemical analysis of plant confirm the presence of macromolecules which function as bio-reductant and stabilize the nanoparticles. The Jr.$NiFe_2O_4$ NPs were characterized by UV-visible, FTIR spectroscopy, PXRD pattern, SEM and TGA/ DTA analysis. The nanoparticles proved to be optically active having a value of indirect bandgap of energy in the range of 1.53 eV. Besides, the ciprofloxacin (CIP) and Congo red (CR) degradation ability of Jr.$NiFe_2O_4$ NPs were also discussed. It is seen that the highest degradation

rate was acquired for CIP using pH = 3, at 254 nm, while 85 % of removal rate was analysed for CR. The kinetic studies in case of CR removal followed pseudo-first-order. Overall, these data recommend an innovative inspiring application of a plant-mediated synthesis of Jr.$NiFe_2O_4$ NPs.

Keywords
Bio template; Spinel ferrite; Optical activity; Degradation; Ciprofloxacin; Congo red

1. Introduction

Water plays a key role in everyday life but the unconstrained release of organic pollutants in water produces an extremely dangerous effect on human beings as well as on aquatic life. It has been seen that the conventional way of wastewater treatment leads to the production of wastewater-borne microorganisms to higher concentrations of Fluoroquinolones (FQ)[1]. A minimum inhibition concentration of the most famous and powerful second-generation FQ, ciprofloxacin (CIP) has been continuously found in wastewater and induce bacterial resistance and many side effects like neurological disorder and ruptured tendons. According to many studies ciprofloxacin (CIP) can be degraded or removed from the wastewater by adsorption applications and advanced oxidation processes (AOPs) including sonification, ozonation, photolysis and heterogeneous photocatalysis[2].

On the other hand, highly developed industrialization and unrestrained discharge of organic dyes is the major cause of water contamination[3]. One of the most utilized dyestuffs is azo dyes having –N=N- linkage bonded to aromatic rings. The azo dyes such as Congo red (CR) dye is extensively used in the fabric industry[4,5]. [5]. Several approaches are adopted for degradation of CR dye like adsorption, coagulation, ion exchange, chemical oxidation and biodegradation etc[6-8]. However heterogeneous photolysis technique is considered the most propitious approach to destabilize organic pollutant from water. Initiation of photocatalysis decontamination of dyes favours the expense efficacious strategy in the use of sustainable energy system[4,9].

Nowadays, nanomaterials of various forms, shape and morphologies, e.g., carbonaceous nanomaterials, dendrimers, carbon nanotubes, zeolites, nanofibers and metal-containing nanoparticles have been widely employed for wastewater treatment[10]. However, the recyclability of these materials is a fundamental problem due to their nano size[10]. This problem is overwhelmed using magnetic

nanoparticles (MNPs) materials which can be easily recycled by the application of magnetic filtration. The variety of magnetic nanomaterial composites like Fe@SiO_2, Fe_3O_4@C, Fe_3O_4@TiO_2, PEO (poly(ethylene oxide)Fe_3O_4@PPO (poly(propylene oxide)), Fe_3O_4@PNIPAM (poly(N-isopropylacrylamide)),Fe_3O_4@PDA (polydopamine), Fe_3O_4@CNTs (multiwalled carbon nanotubes), Fe_3O_4@MIPs (molecularly imprinted polymer-encapsulated particles), iron oxide-oxyhydroxide/rGO, Fe@CS (carbon spheres), etc. have been used for wastewater treatment[11]. The spinal ferrites and its derivatives are famous for the remediation of various water pollutants[12]. Recently magnetic poly (styrene-2-acrylamido-2-methyl propanesulfonic acid) and magnetic (1,2,4,5-benzenetetracarboxylic acid) nanomaterials have been proved very effective for the removal of pharmaceuticals viz. atenolol, diclofenac sodium and ceftriaxone sodium and Congo red dye from water respectively[13,14]. The surface modification of magnetic nanoparticles is a quite simple and cost-effective approach which fall in the category of desired applications. The fabricated magnetic nanoparticles formed as an inorganic-organic blend by connecting organic species on the inorganic sideshow mechanical stability due to inorganic core and flexibility in solution due to organic modifications. By taking the advantages of magnetic nanoparticles, we synthesized $NiFe_2O_4$ by using the leaf extract of *Juglans regia*. The green strategy has been adopted to contrive metal oxide-containing spinel ferrites by using numerous plants, for instance, rambutan, Malachra capitata, Mirabilis jalapa, lemon eucalyptus, Hibiscus rosa-sinensis black nightshade neem[15-22]. According to our literature survey, there is no report of *Juglans regia* leaves extract mediated synthesis of nickel ferrite nanoparticles (Jr.$NiFe_2O_4$ NPs) and it's potential to remove the ciprofloxacin and Congo red dye from water, which is the subject of this paper. Furthermore, the physio and phytochemical analysis of *Juglans regia* leaves and the extract is also discussed.

2. Materials and methods

2.1. Materials

Jr.$NiFe_2O_4$ NPs were synthesized by utilizing the following precursors; Nickle Nitrate Tetrahydrate *($Ni(NO_3)_2.4H_2O$, 99.99% Sigma-Aldrich); Iron(III) nonahydrate ($Fe(NO_3)_3.9H_2O$, 98% Sigma-*Aldrich); Sodium Hydroxide pellets(NaOH, 98% Sigma-Aldrich); Ammonium hydroxide (NH_4OH, 99.99% Merck); Sulphuric Acid (H_2SO_4, 98% Sigma-Aldrich); Chloroform ($CHCl_3$, 99.99% Sigma-

Aldrich); Hydrochloric acid (37 wt% in H_2O Sigma-Aldrich); Ciprofloxacin ($C_{17}H_{18}FN_3O_3$, 99% Sigma-Aldrich). The dye used for photolysis was Congo red ($C_{32}H_{22}N_6Na_2O_6S_2$, Sigma-Aldrich); All chemicals were used as received.

2.2. Physiochemical Analysis of *Juglans regia* leaves

The physicochemical analysis was carried out by following the guidelines and protocols (in triplicates) approved by the WHO[23].

2.2.1. *Macroscopic analysis*

In the preliminary step, an organoleptic investigation was performed using the sense of organ to outline the nature and basic parameters of the flower extract.

2.2.2. Determination of moisture content (loss on drying)

10 grams of the leaves were taken in moisture dish and initially air-dried followed by oven-drying at 105–110°C for 20 minutes to remove water contents completely. The weight loss (mg/g) was determined by total moisture content.

$$\text{Moisture content (\%)} = \frac{Initial\ weight\ of\ leaves - Oven\ dry\ weight\ of\ leaves}{Oven\ dry\ weight\ of\ leaves}\ X\ 100 \quad \text{(Eq. 1)}$$

2.2.3. Estimation of total ash

Around 2 grams of leaves were taken in the crucible and extend in layers onto the crucible. The material burnt at 500 – 600 °C. The white residue of the leaves was due to the non-existent carbon. The percentage of ash content was calculated by the following.

$$Ash\ content\ (\%) = \frac{Weight\ of\ ash}{Weight\ of\ sample\ taken}\ X\ 100 \quad \text{(Eq. 2)}$$

2.2.4. *Estimation of acid-insoluble ash*

The ash contents obtained from crucible were blended with 2M HCl (25 mL) and covered with a watch glass. The mixture was boiled for 5 minutes and the acid-insoluble contents were obtained by filtering the reaction mixture through ashless filter paper. After that washed the filter paper with hot water, dried, ignited and weighed.

$$Acid\ insoluble\ ash\ (\%) = \frac{Weight\ of\ acid\ insouble\ content}{Weight\ of\ total\ ash}\ X\ 100 \quad \text{(Eq. 3)}$$

2.2.5. Estimation of water-soluble ash

The ash contents were taken in a crucible and 25 mL water was added to it and covered with a watch glass. The reaction mixture was boiled for 5 minutes and the water-insoluble contents were obtained on ashless filter paper, ignited at elevated temperature. The weight of water-soluble ash was

calculated by subtracting the weight of water-insoluble ash from the weight of total ash. The following formula was used to calculate the percentage of water-soluble ash.

$$Water\ soluble\ ash\ (\%) = \frac{Weight\ of\ water\ soluble\ ash}{Weight\ of\ total\ ash}\ X\ 100 \qquad \text{(Eq. 4)}$$

2.3. Quantitative phytochemical screening of *Juglans regia* leaves

2.3.1. Estimation of alcohol-soluble extractive

In a round-bottomed flask, 5 g of the material was dissolved in 100 mL of ethanol (90 %) and shook on an electrical shaker for 6 hours. After 12-hour maceration the reaction mixture was filtered. The filtrate was dried to calculate the weight of the alcohol-soluble extract. The percentage of alcohol-soluble extractive was determined by the following formula.

$$Alcohol\ soluble\ extractive\ (\%) = \frac{Weight\ of\ extract}{Weight\ of\ sample}\ X\ 100 \qquad \text{(Eq. 5)}$$

2.3.2. Estimation of water-soluble extractive

In a round-bottomed flask, 5 g of the finely powdered leaves were dissolved in water (100 mL) and shook on an electrical shaker for 6 hours. After 12-hour maceration the reaction mixture was filtered. The filtrate was dried to calculate the weight of the water-soluble extract. The percentage of water-soluble extractive was determined by the following formula.

$$Water\ soluble\ extractive\ (\%) = \frac{Weight\ of\ extract}{Weight\ of\ sample}\ X\ 100 \qquad \text{(Eq. 6)}$$

2.4. Quantitative phytochemical screening of *Juglans regia* leaves

2.4.1. Preparation of leaves extract

The *Juglans regia* leaves were initially ground to fine powder followed by hot continuous extraction in a Soxhlet extractor, with various known solvents (nonpolar to polar). Before extracting with the next solvent, leaves powder was dried at less than 50°C in a warm air oven. All the fractions were mixed, concentrated in a water bath, and stored in the refrigerator for qualitative analysis and synthesis of ferrites nanoparticles.

2.4.2. Characterization of phytochemicals

Plants are considered as biosynthetic laboratory having a variety of organic compounds which the medicinal value of that plant. The qualitative identification of these organic compounds in *Juglans regia* leaves extract was conducted according to the conventionally practised procedure.

2.4.3. Test of tannins

1 mL of extract was further diluted with 20 mL of water and boiled in a vial and then filtered. In the filtrate 0.1% $FeCl_3$ solution was added and the appearance of brownish-green colouration showed the presence of tannins.

2.4.4. Test of saponin

In 2 mL of the extract, 20 mL of water was mixed with water and boiled for 15 minutes under continuous stirring. The layer of foam formed, showed the presence of saponin.

2.4.5. Test of flavonoids

In a reaction vial, 2 mL of extract, NH_4OH and concentrated H_2SO_4 (5 mL each) were mixed and placed undisturbed. The appearance of yellow colouration authenticated the presence of flavonoids.

2.4.6. Test of steroids

To 2 mL of extract, H_2SO_4 and acetic anhydride (2 mL each) were mixed in a test tube and reaction mixture. No change in colour from violet to bluish green showed the absence of steroids in the extract.

2.4.7. Test of terpenoids

The terpenoid content was determined by mixing 5 mL of the extract with chloroform (2 mL) and concentrated H_2SO_4 (3 mL). The reaction mixture was continuously stirred but no reddish-brown colour is seen which showed the absence of terpenoids or terpenes.

2.4.8. Test of triterpenoids

In a test tube, acetic anhydride, the extract, chloroform (1 mL each) and concentrated H_2SO_4 (2 mL) were thoroughly mixed. The solution did not turn reddish violet which showed the absence of triterpenoids in the extract.

2.4.9. Test of alkaloids

One mL of extract was mixed with a few drops of Mayer's reagent. The formation of white precipitates showed the presence of alkaloids.

2.4.10. Test of polyphenols

The mixture of extract (1 mL) and ethanol (4 mL) was initially boiled followed by the addition of 2-3 drops of ferric cyanide solution. The appearance of a bluish-green colour confirmed the presence of polyphenol.

2.4.11. Test of anthraquinones

In a reaction vial, of 5 mL extract, dilute H_2SO_4, benzene and dilute NH_4OH(1 mL each) were mixed and the emergence of rose-pink colouration confirmed the presence of anthraquinones.

2.4.12. Test of glycosides

To the 1 mL of the extracts, 1 mL of conc. sulphuric acid was added and allowed to stand for 2 min. a reddish colour precipitate showed the presence of glycosides.

2.4.13. Test of coumarins

To 3 mL of extract, 2 mL of 10% NaOH was added. No yellow colouration confirmed the absence of coumarins.

2.5. Synthesis of Jr.$NiFe_2O_4$ NPs

Jr.$NiFe_2O_4$ NPs were developed by using metal nitrates as precursors via hydrothermal approach and prepared *Juglans regia* leaf extract as the stabilizing agent. $Ni(NO_3)_2.4H_2O$ and $Fe(NO_3)_3.9H_2O$ was mixed in the ratio of 1:2 with dropwise addition of 70 mL of the plant extract. The suspension was flowed into an autoclave tube and heated at 200°C for 2 h. Then formed precipitates were subjected to filtration and washed with distilled water to keep neutral pH and dried in an oven for 60 minutes at 100°C. To determine the annealing effect on the particle size of Jr.$NiFe_2O_4$ NPs, the precipitates were finely ground and annealed at different temperature (600– 1200°C) under air atmosphere for different time intervals (2 -10 hours).

2.6. Characterization techniques

2.6.1. UV-Visible spectroscopy

The formation of Jr.$NiFe_2O_4$ NPs by reduction of silver nitrate into silver ion was confirmed by UV-Visible spectroscopy (Cecil 7500 UV-vis spectrophotometer). The data was recorded from 200 to 800 nm.

2.6.2. Morphological analysis

Field Emission Scanning Electron Microscope (SEM) MIRA-III TESCON was employed to observe the morphology of Jr.$NiFe_2O_4$ NPs. The samples were carbon coated and their morphology was probed using FESEM working at an operating voltage of 20 kV.

2.6.3. PXRD analysis

The crystallite size of Jr.$NiFe_2O_4$ NPs was determined by Powder X-ray Diffractometer (Bruker D8 Advance PXRD) with high-resolution LynxEye detector and a Cu radiation source.

2.6.4. FT-IR

Fourier Transform Infra-Red Spectrometer (Bruker Tensor 27 FTIR) was used for the determination of respective metal salts into Jr.$NiFe_2O_4$ NPs by reducing agent present in aqueous extract of *Juglans regia.* The data were collected in the range of 400 to 4000 cm^{-1}.

2.6.5. Thermal analysis

The thermogravimetric and differential thermal analysis of the contrived Jr.$NiFe_2O_4$ NPs from green method was exercised through the thermal analyser (TA instrument, SDT Q600) to investigate the decay and temperature of crystallization.

2.6.6. Statistical analysis

Microsoft excel, origin software's were used for statistical analysis. The data was collected with average +/- standard deviation after performing an experiment in the form of triplicates."

2.7. Removal of Ciprofloxacin (CIP) by Jr.$NiFe_2O_4$ NPs

The removal of CIP from the water was conducted at different pH by using diverse UV lamps working at varying wavelengths, aimed to predict the wavelength at which maximum degradation of CIP could obtain. It was checked that 1 hour of reaction time was enough to degrade CIP to its maximum, but the reaction was performed for 70 minutes to confirm that no more observable CIP concentration was degraded in extra 10 minutes. It was seen that the increased degradation rate was acquired for CIP using pH = 3, at 254 nm than longer 365 nm wavelength. Same conditions were applied for all reactions with UV visible spectrometer. Rate constant was also calculated from kinetic facts at varying pH by using a kinetic equation which was employed for batch reactions.

$$Rate\ of\ degradation = -\frac{d[A]}{dt} = k[A] \qquad \text{(Eq. 7)}$$

Where

$$[A] = concentration\ of\ CIP\ \left(\frac{mg}{L}\right)$$

$$t = time\ (min)$$

$$k = rate\ constant\ (1/min)$$

The integrated form of the above equation is.

$$\ln[A] = -kt + \ln[A]_o \qquad \text{(Eq. 8)}$$

2.8. Removal of Congo red (CR) by Jr.NiF_2O_4 NPs

JR.$NiFe_2O_4$ NPs was employed as photocatalyst for the reduction of one of the azo dyes, Congo red (CR) worked as a testing model under visible light. Degradation reaction was performed by using the 5mg L^{-1} solution of Congo red in deionized water with 5 mg of prepared catalyst, aimed to evaluate degradation of organic effluent at a lower concentration. In commencement, the adsorption-desorption equilibrium was created by stirring the solution under dark for 30 minutes. After its establishment, 2 mL of suspension was removed to see the absorption peak. The solution was stirred under sunlight at noon when light intensity is high. It was stirred continuously for 75 minutes and 2 mL of the mixture was detached after every 15 minutes interval to measure absorption spectra. The discharged rate was determined by applying the following formula.

$$\%age\ removal = \frac{A_o - A_t}{A_o}\ X\ 100 \qquad \text{(Eq. 9)}$$

A_o= absorbance at time "0"

A_t = absorbance after 15 minutes interval

3. Results and Discussion

3.1. Physio and Phytochemical analysis

The *Juglans regia* leaves extract played a significant role in manipulating the bioconjugate Jr.$NiFe_2O_4$ NPs. The organic compounds used in the formation and stabilization of ferrite nanoparticles have easily tacit through physio and phytochemical analysis of *Juglans regia* leaves extract. The basic attributes of *Juglans regia* leave extract were expressed in terms of percentage including moisture content (2.03%); total ash content (4.98%); acid-insoluble ash (0.86%), water-soluble ash (6.2%); alcohol-soluble extractives (8.1%); and water-soluble extractives (9.54%).

These results of phytochemical analyses supported the water-soluble extractive method owing to its easy procedure and cost-effectiveness. The qualitative results of the phytochemical analysis revealed

the presence of high concentrative components including triterpenoids (18.87%); tannins (18.28%); glycoside (16.98%); steroids (16.56%), and (14.36%). Whereas the saponins (5.88%) and alkaloids (9.07%) were present in low concentrations. The terpenoids, coumarins, triterpenoids and steroids were absent. The results signify the major contribution of *Juglans regia* leaves extract in the formation of Jr.$NiFe_2O_4$ NPs.

3.2. UV-Visible Spectroscopy

The UV-visible graph of nickel ferrite samples S1 (Jr.$NiFe_2O_4$) and S2 to S6 annealed at different temperature 600- 1200°C are depicted in Fig. 1. Absorption spectra of small nanoparticles less than 20nm are in the range of 323-350nm wavelength usually with a single sharp band. As the size of nanoparticles increases redshift seen due to light scattering process. The shape, environment and composition of the prepared nanoparticles affect the scattering of light. The sample S6 annealed at 1200 degree showed two absorption bands at 372nm and 484nm because of larger size nanoparticles. Higher dispersion was observed as the annealing temperature increased from 600- 1200°C that is consistent with the size increasing upon calcination[24].

Fig. 1 Ultraviolet-Visible spectrum of Nickel ferrite of samples S1 (Jr.$NiFe_2O_4$) and S2 to S6 annealed at different temperature.

3.3. Fourier Transform Spectroscopy

FT-IR spectra of synthesized nickel ferrite, S1 (Jr.$NiFe_2O_4$) and annealed nickel ferrites (S2-S6) are depicted in Fig. 2. Ferrites nanoparticles show two fundamental absorptions bands. One because of stretching vibrations of metal-oxygen (M-O)bond in octahedral sites and other band is allotted to Stretching vibration of M-O bond in the tetrahedral site which is a characteristic of spinel ferrites. The small band appeared at 2861 cm^{-1} is ascribed to the C-C bond or C-O bond due to organic impurities [25,26]. As annealing temperature has increased the impurities was burned out and the peak was disappeared. Some minor bands near 1600 region appeared because of stretching frequencies of H-O-H of free or adsorbed H_2O molecules [27,28]. Three major and characteristics peaks are seen are at 607,

489, and 484 cm-1 which indicate the formation of nickel ferrite consistent with the XRD results. These characteristics peaks are attributed to the M-O stretching vibrations [29].

Fig. 2 FTIR spectrum of nickel ferrite samples S1 (Jr.$NiFe_2O_4$) and S2 to S6 annealed at different temperature.

3.4. X-Ray Diffraction Spectroscopy (XRD)

The lattice framework and recognition of the crystalline nature of the Jr.$NiFe_2O_4$ NPs were determined by XRD (Bruker D8-advance, Germany). The XRD patterns were achieved by steps of 0.028 ranging from 108 _ 2u _ 708 in 0.1second per step at ambient temperature. PXRD utilizing Cu-Ka with wavelength 1.5425 Å, radiation (D8, Advance, Bruker) was engaged to examine phase formation and purity. Step size 0.5 Sec/step and increment in 2θ is 0.02 although ferrite generates fluorescence with copper source, results are fine enough. XRD graph explains features of synthesized nickel ferrite nanoparticles. Especially the effect of annealing on phase contribution and increase in crystallize size. The crystalline phase of the Nickel ferrite samples was analysed through qualitative XRD patterns.

Different XRD patterns were seen for samples annealed at different temperature by keeping the time constant likewise developing crystalline phase was shown of the sample annealed for 2 hours as depicted in Fig. 3. The confirmation for the development of nickel ferrites was attained by comparing the results of the diffractograms with literature JCPDS files. Very sharp and broad peaks of the sample on diffractograms convince for the ultra-fine and pure structure of the nickel ferrite. The diffraction patterns associated with interplanar spacing between (220), (311), (222), (400), (422), (511), (440) and (533) planes of the spinel Jr.$NiFe_2O_4$ NPs with cubic symmetry[30].

Two more peaks were seen at diffraction pattern of (104) and (024) which were indexed to β-Fe_2O_3. The other peaks were expected because of the presence of an excess of oxygen during the annealing process. In detail, two peaks at 2θ 24.12 and 49.36 are referred to β-Fe2O3. The additional peaks revealed the development of a minor phase beside the major phase of nickel ferrite in sample S3 and S4 that was annealed at 800°C and 900°C respectively. The minor phase is considered as an intermediate phase that usually appears during the formation of nickel ferrite. But as the annealing

temperature was raised to 1200°C the minor phase diffraction peaks disappeared as the nickel ferrite phase or major phase was fully developed. Crystallite size determined manually using Debye-Scherrer's formula(Eq. 10). The results are cross-checked by using area plot in Eva software.

$$t = \frac{K\lambda}{\beta cos\theta} \qquad \text{(Eq. 10)}$$

t = grain size

K = constant having value 0.89

λ = wavelength equal to 0.154nm

B = full width at half maxima

θ = diffracted angle

The powder XRD patterns of Jr.$NiFe_2O_4$ NPs obtained reveal the cubic morphology of Jr.$NiFe_2O_4$ NPs and compared with the standard pattern. All the standard based reflections were indexed. The presence of hematite diffraction peaks contributes as an impurity reveals the formation of a multi-phase. The sample S5 and S6 not showing the presence of hematite phase but the DRS spectra show an extra line of bandgap energy. It may be because of fluoresces due to which the phase contribution of hematite is ignorable. It is seen that the lattice parameters for all samples are identical [8.337 Å], consider good as compare to standard $NiFe_2O_4$ value (8.34Å).

Fig. 3 XRD patterns of samples (Jr.$NiFe_2O_4$) and S2 to S6 annealed at different temperature and for different periods

3.5. Morphology study

The grain size, surface morphology, and shape of the Jr.$NiFe_2O_4$ Nps were monitored through SEM (Fig 4). The agglomeration of nanoparticles was observed which is due to plant phytochemicals and secondary metabolites. The average grain size of Jr.$NiFe_2O_4$ Nps was founded in the range of 1-2 μm.

The synthesis of nanoparticles was due to the interaction between capping biomolecules and nickel ferrite through an electrostatic bond or hydrogen bond.

Fig. 4 Scanning electron micrographs of Jr.$NiFe_2O_4$ Nps

3.6. Optical Results

3.6.1. Tauc Plot for illustration of the bandgap

(1) Tauc plot was used for bandgap assessment from DRS with the help of the equation suggested by Tauc, Davis and Mott.

$$(ahv)^{1/n} = A(hv - Eg) \qquad \text{(Eq. 11)}$$

Where

"h" is the Planck's constant, "ν" is the frequency of the photon, "α" is the absorption coefficient,

"Eg" is the energy of bandgap, "A" is the constant and "n" is the nature of the transition.

For direct allowed transition.....n = 1/2

For direct forbidden transition.....n = 3/2

For indirect allowed transition.....n = 2

For indirect forbidden transition.....n = 3

Since the indirect allowed sample transition is used in this work, n =2 is used for the Jr.$NiFe_2O_4$ NPs

(2)The obtained DRS is changed to the Kubelka-Munk function. Thus, the vertical axis is converted to quantity F(R∞), which is proportional to the "α". F(R∞) is then placed in the equation instead of constant "α".So, the final equation becomes.

$$(hvF(R\infty))^{1/2} = A(hv - Eg) \qquad \text{(Eq. 12)}$$

(3) A plot of $(hvF(R\infty))^{1/2}$verses hν is attained by using the Kubelka-Munk function. The curve of $(hv-(hvF(R\infty))^{1/2})$ on the horizontal axis hν and a vertical axis $(hvF(R\infty))^{1/2}$ is obtained. Here, eV is the unit of hν and associated with λ ashν= 1239.7/λ.

(4) At the point of inflexion, a line is made tangent on the curve of step 3 and the hν value at the point of intersection of the tangent line and the horizontal axis is the Eg value.

The curve that is the value of $(hv- (hvF(R\infty))^{1/2})$ and the respective tangent, related to the procedures of steps (3) and (4), are depicted for each sample in Fig. 5a,b. The value related to the crossing point

of the line tangent to the plotted curve inflexion point with the horizontal axis (hν axis) becomes the bandgap Eg value.

Fig. 5a Reflectance spectra of samples annealed at different

Optical results of Nickle ferrites are very fantastic and according to literature. Sample S1 ($Jr.NiFe_2O_4$) and remaining S2-S6, 600, 800, 900, 1000 and 1200 °C respectively. Hematite phase present which already confirmed from XRD data. The second bandgap is due to the presences of hematite. Although sample S6 not annealed separately as others it collected after TGA/DTA Analysis (1200°C) showing that only $Jr.NiFe_2O_4$ NPs present and no other bandgap energy line. For the measurement of reflectance spectra, the quantity of S6 is ridiculously small as compared to others, it may be a reason for small reflectance value. The value of indirect bandgap of energy for $Jr.NiFe_2O_4$ NPs is found to be in the range of 1.53 eV and for hematite in range of 1.82–1.96 eV.

Fig. 5b Reflectance spectra of $Jr.NiFe_2O_4$ samples annealed at different temperature

3.7. Thermal analysis

The two techniques (TGA-DTA) collectively used for determination of $Jr.NiFe_2O_4$ NPs thermal behaviour. While weighing loss of samples were evaluated via TG, DTA also examine material characteristics where no weight loss occurs, e.g. change in crystal composition, liquefying, glass transition etc

The TG curve (Fig. 6) shows a small weigh loss steps from 100 ºC to 270 ºC and vital decay steps from 270 ºC to 420 ºC. Up to 1200 °C, noticeable decomposition was not seen. The slight weight decay was due to moisture loss and trapped solvent in the $Jr.NiFe_2O_4$ NPs while the combustion of organic PAN matrix causes great mass loss. TG curve shows the plateau between 450ºC to 1200 ºC which divulge the crystalline $Jr.NiFe_2O_4$ NPs synthesis.

Fig. 6 TGA/ DTA graph of $Jr.NiFe_2O_4$ Nps

3.8. Removal of Ciprofloxacin

It was revealed from kinetic details that 1 hour of the experiment was enough to reach maximum degradation depicted in Fig. 7a,b.

Linear line with an incline of –k was obtained because of the plot of the natural log of final concentration verse time which showed that the reaction was first order shown in Fig. 8a,b. Rate constants for pH 3, 7 and 10 were 0.0461/min (R^2 = 0.946), 0.0389/min (R^2 = 0.953) and 0.0297/min (R^2 = 0.893) respectively which showed that rate constant values decreased with increase of pH. Rate of reaction found to be decreased to zero after 1 hour under UV light irradiation with the first concentration of 20mg/L because most of CIP amount degraded after 60 minutes. So, the decrease in reaction rate was seen. Consumption of oxygen, being a limiting reactant in water may also be another reason for the reduction of reaction rate. It was observed that the removal rate of CIP having pH 3was enhanced at 254 nm than longer 365 nm wavelength.

Fig. 7a Degrading potency of Jr.$NiFe_2O_4$ NPs (CIP conc. Verses time graph)

Fig. 7b Degrading potency of Jr.$NiFe_2O_4$ NPs (ln CIP conc. vs time graph)

Fig. 8a Degrading potency of Jr.$NiFe_2O_4$ NPs (Kinetic plot of $-\ln(C/C_o)$ vs time)

Fig. 8b Degrading potency of Jr.$NiFe_2O_4$ NPs (Kinetic plot of C/C_o vs time)

3.9. Removal of Congo red (CR) dye

Evaluation of photocatalytic experiment for the removal of CR was conducted via UV-visible spectroscopy shown in Fig. 9,10. It was seen that the intensity of the absorption band of CR at 498 nm was decreased gradually as exposed to sunlight for 75 minutes. 85 % of removal rate was analysed for CR which showed remarkable photocatalytic activity of Jr.$NiFe_2O_4$ NPs.

Fig. 9 Absorption Spectra of CR dye at different time intervals

The phenomenon of photocatalysis involved the transition of electrons from a ground state to excited state when light intensity is absorbed by the catalyst, leading to the production of valence band hole (h^+_{VB}) and conduction band electron (e^-_{CB}). Light-induced electrons (e^-_{CB}) covert the molecular oxygen into superoxide radical ($O_2^{\bullet}$) and hydroxyl radicals are generated by reacting water molecules with a highly oxidizing hole (h^+_{VB}). Valence band hole (h^+_{VB}) has greater strength to draw electrons of CR dyestuff which lead to the degradation of contaminant. Therefore, it can be concluded that Hole (h^+_{VB}) and radicals generated during the phenomenon are the main species to detoxify the organic dye [31].

Fig. 10 Degradation rate of CR under visible light irradiation

Kinetic studies were also conducted for estimating the rate of reaction for photocatalytic activity. Straight-line showed that degradation experiment followed pseudo-first-order kinetics as shown in Fig. 11a,b. Following equation described the kinetic process.

$$ln\frac{A_o}{A_t} = kt \qquad \text{(Eq. 13)}$$

A_o= Initial absorbance of CR

A_t= Absorbance of CR after 15 minutes intervals

K = Rate constant

Fig. 11a Kinetic plot for degradation of CR, a plot of $-\ln(A_t/A_o)$ vs time

Fig. 11b Kinetic plot of degradation of CR, a plot of A_t/A_o vs time

4. Conclusion

Here, for the first time, we describe that *Juglans regia* leaves extract is a valued source for bio-conjugated nickel ferrite nanoparticles (Jr.$NiFe_2O_4$ NPs) in an eco-friendly way. The bandgap value of 1.53 eV makes the synthesized Jr.$NiFe_2O_4$ NPs are optically active. The Jr.$NiFe_2O_4$ NPs showed excellent ability in the removal of ciprofloxacin and Congo red from the water. It is seen that the ciprofloxacin maximally degraded under highly acidic condition (pH = 3) at 254 nm than longer 365 nm. The Jr.$NiFe_2O_4$ NPs have the excellent ability to bump off the CR up to 80 percent. The kinetic studies recommend the pseudo-first-order kinetic model. The results make the Jr.$NiFe_2O_4$ NPs a promising photocatalyst for the water purification.

Conflict of interest

There is no conflict of interest between the authors

References

1 Naidoo, S. & Olaniran, A. O. Treated wastewater effluent as a source of microbial pollution of surface water resources. *International journal of environmental research and public health* **11**, 249-270 (2014).

2 Salimi, M. *et al.* Contaminants of emerging concern: a review of new approach in AOP technologies. *Environmental monitoring and assessment* **189**, 414 (2017).

3 Pan, S. *et al.* Optimization on Adsorption Process of Congo Red onto Magnetic Ni0. 5Cu0. 5Fe2O4/SiO2 Nanocomposites and Their Adsorption Mechanism. *Journal of nanoscience and nanotechnology* **20**, 789-801 (2020).

4 Yaneva, Z. L. & Georgieva, N. V. Insights into Congo Red Adsorption on Agro-Industrial Materials- Spectral, Equilibrium, Kinetic, Thermodynamic, Dynamic and Desorption Studies. A Review. *International Review of Chemical Engineering* **4**, 127-146 (2012).

5 Zhang, Y. *et al.* High efficiency reductive degradation of a wide range of azo dyes by SiO2-Co core-shell nanoparticles. *Applied Catalysis B: Environmental* **199**, 504-513 (2016).

6 Afkhami, A., Sayari, S., Moosavi, R. & Madrakian, T. Magnetic nickel zinc ferrite nanocomposite as an efficient adsorbent for the removal of organic dyes from aqueous solutions. *Journal of Industrial and Engineering Chemistry* **21**, 920-924 (2015).

7 Chen, R. *et al.* Rapid hydrothermal synthesis of magnetic CoxNi1− xFe2O4 nanoparticles and their application on removal of Congo red. *Chemical Engineering Journal* **242**, 226-233 (2014).

8 Fowsiya, J., Madhumitha, G., Al-Dhabi, N. A. & Arasu, M. V. Photocatalytic degradation of Congo red using Carissa edulis extract capped zinc oxide nanoparticles. *Journal of Photochemistry and Photobiology B: Biology* **162**, 395-401 (2016).

9 Byrne, C., Subramanian, G. & Pillai, S. C. Recent advances in photocatalysis for environmental applications. *Journal of Environmental Chemical Engineering* **6**, 3531-3555 (2018).

10 Singh, R. & Dutta, S. in *Handbook of Research on Emerging Developments and Environmental Impacts of Ecological Chemistry* 307-324 (IGI Global, 2020).
11 Sharma, M., Kalita, P., Senapati, K. K. & Garg, A. Study on Magnetic Materials for Removal of Water Pollutants. *Emerging Pollutants: Some Strategies for the Quality Preservation of Our Environment*, 61 (2018).
12 Kumar, A., Sharma, G., Naushad, M. & Thakur, S. SPION/β-cyclodextrin core–shell nanostructures for oil spill remediation and organic pollutant removal from waste water. *Chemical Engineering Journal* **280**, 175-187 (2015).
13 Chatterjee, S. *et al.* Selective and Recyclable Congo Red Dye Adsorption by Spherical Fe 3 O 4 Nanoparticles Functionalized with 1, 2, 4, 5-Benzenetetracarboxylic Acid. *Scientific Reports* **10**, 1-11 (2020).
14 Hayasi, M. & Saadatjoo, N. Preparation of magnetic nanoparticles functionalized with poly (styrene-2-acrylamido-2-methyl propanesulfonic acid) as novel adsorbents for removal of pharmaceuticals from aqueous solutions. *Advances in Polymer Technology* **37**, 1941-1953 (2018).
15 Laokul, P., Amornkitbamrung, V., Seraphin, S. & Maensiri, S. Characterization and magnetic properties of nanocrystalline CuFe2O4, NiFe2O4, ZnFe2O4 powders prepared by the Aloe vera extract solution. *Current Applied Physics* **11**, 101-108 (2011).
16 Srirangam, G. & Rao, K. P. SYNTHESIS AND CHARCTERIZATION OF SILVER NANOPARTICLES FROM THE LEAF EXTRACT OF MALACHRA CAPITATA (L.). *Journal of Chemistry* **10**, 46-53 (2017).
17 Yuvakkumar, R., Suresh, J., Nathanael, A. J., Sundrarajan, M. & Hong, S. Rambutan (Nephelium lappaceum L.) peel extract assisted biomimetic synthesis of nickel oxide nanocrystals. *Materials Letters* **128**, 170-174 (2014).
18 Zheng, Y. *et al.* Green biosynthesis and characterization of zinc oxide nanoparticles using Corymbia citriodora leaf extract and their photocatalytic activity. *Green Chemistry Letters and Reviews* **8**, 59-63 (2015).
19 Gopalakrishnan, M., Sheenu, A., Varghese, B., Dharani, J. & Saranya, S. A GREEN APPROACH FOR SYNTHESIS AND CHARACTERIZATION OF SILVER NANOPARTICLESAND THEIR ANTI-MICROBIAL ACTIVITY.
20 Ramesh, M., Anbuvannan, M. & Viruthagiri, G. Green synthesis of ZnO nanoparticles using Solanum nigrum leaf extract and their antibacterial activity. *Spectrochimica Acta Part A: Molecular and Biomolecular Spectroscopy* **136**, 864-870 (2015).
21 Bhuyan, T., Mishra, K., Khanuja, M., Prasad, R. & Varma, A. Biosynthesis of zinc oxide nanoparticles from Azadirachta indica for antibacterial and photocatalytic applications. *Materials Science in Semiconductor Processing* **32**, 55-61 (2015).
22 Devi, R. S. & Gayathri, R. Green synthesis of zinc oxide nanoparticles by using Hibiscus rosa-sinensis. *Int J Curr Eng Technol* **4**, 2444-2446 (2014).
23 Santos, F. *et al.* Brazilian propolis: physicochemical properties, plant origin and antibacterial activity on periodontopathogens. *Phytotherapy Research* **17**, 285-289 (2003).
24 Rodrigues, A. R. O. *et al.* Magnetic liposomes based on nickel ferrite nanoparticles for biomedical applications. *Physical Chemistry Chemical Physics* **17**, 18011-18021 (2015).
25 Babu, B. R. & Tatarchuk, T. Elastic properties and antistructural modeling for Nickel-Zinc ferrite-aluminates. *Materials Chemistry and Physics* **207**, 534-541 (2018).
26 Kane, S. *et al.* in *AIP Conference Proceedings.* 030089 (AIP Publishing).

27 Naik, M. M. *et al.* Effect of aluminium doping on structural, optical, photocatalytic and antibacterial activity on nickel ferrite nanoparticles by sol–gel auto-combustion method. *Journal of Materials Science: Materials in Electronics* **29**, 20395-20414 (2018).
28 Sharma, R. *et al.* in *AIP Conference Proceedings.* 030117 (AIP Publishing).
29 Iqbal, Y., Bae, H., Rhee, I. & Hong, S. Relaxivities of hydrogen protons in aqueous solutions of PEG-coated rod-shaped manganese-nickel-ferrite (Mn 0.4 Ni 0.6 Fe 2 O 4) nanoparticles. *Journal of the Korean Physical Society* **65**, 1594-1597 (2014).
30 Blanco-Gutiérrez, V. *et al.* Superparamagnetic Behavior at Room Temperature through Crystal Chemistry Modification and Particle Assembly Formation: Zinc and Nickel Ferrite Systems. *The Journal of Physical Chemistry C* **123**, 16973-16981, doi:10.1021/acs.jpcc.9b01898 (2019).
31 Borhade, A. V. & Baste, Y. R. Study of photocatalytic asset of the ZnSnO3 synthesized by green chemistry. *Arabian journal of chemistry* **10**, S404-S411 (2017).

Author contributions statement

Supervision, Conceptualization, methodology and original draft preparation M. B. Taj; software, A. Raheel, Heba Alshatir and S. Noor; photocatalytic activity, S.Aroob; Analysis, S. Shabbir and R. H. Ahmad; plant data, R. Fatima; figures preparation, M. D. F. Kahtani; All authors have read and agreed to the published version of the manuscript

Figure ligands

Fig. 1 Ultraviolet-Visible spectrum of Nickel ferrite of samples S1 (Jr.$NiFe_2O_4$) and S2 to S6 annealed at different temperature.

Fig. 2 FTIR spectrum of nickel ferrite samples S1 (Jr.$NiFe_2O_4$) and S2 to S6 annealed at different temperature.

Fig. 3 XRD patterns of samples (Jr.$NiFe_2O_4$) and S2 to S6 annealed at different temperature and for different periods

Fig. 4 Scanning electron micrographs of Jr.$NiFe_2O_4$ Nps

Fig. 5a Reflectance spectra of samples annealed at different

Fig. 5b Reflectance spectra of Jr.$NiFe_2O_4$ samples annealed at different temperature

Fig. 6 TGA/ DTA graph of Jr.$NiFe_2O_4$ Nps

Fig. 7a Degrading potency of Jr.$NiFe_2O_4$ NPs (CIP conc. Verses time graph)

Fig. 7b Degrading potency of Jr.$NiFe_2O_4$ NPs (ln CIP conc. vs time graph)

Fig. 8a Degrading potency of Jr.$NiFe_2O_4$ NPs (Kinetic plot of $-\ln(C/C_o)$ vs time)

Fig. 8b Degrading potency of Jr.$NiFe_2O_4$ NPs (Kinetic plot of C/C_o vs time)

Fig. 9 Absorption Spectra of CR dye at different time intervals

Fig. 10 Degradation rate of CR under visible light irradiation

Fig. 11a Kinetic plot for degradation of CR, a plot of $-\ln(A_t/A_o)$ vs time

Fig. 11b Kinetic plot of degradation of CR, a plot of A_t/A_o vs time

Figures

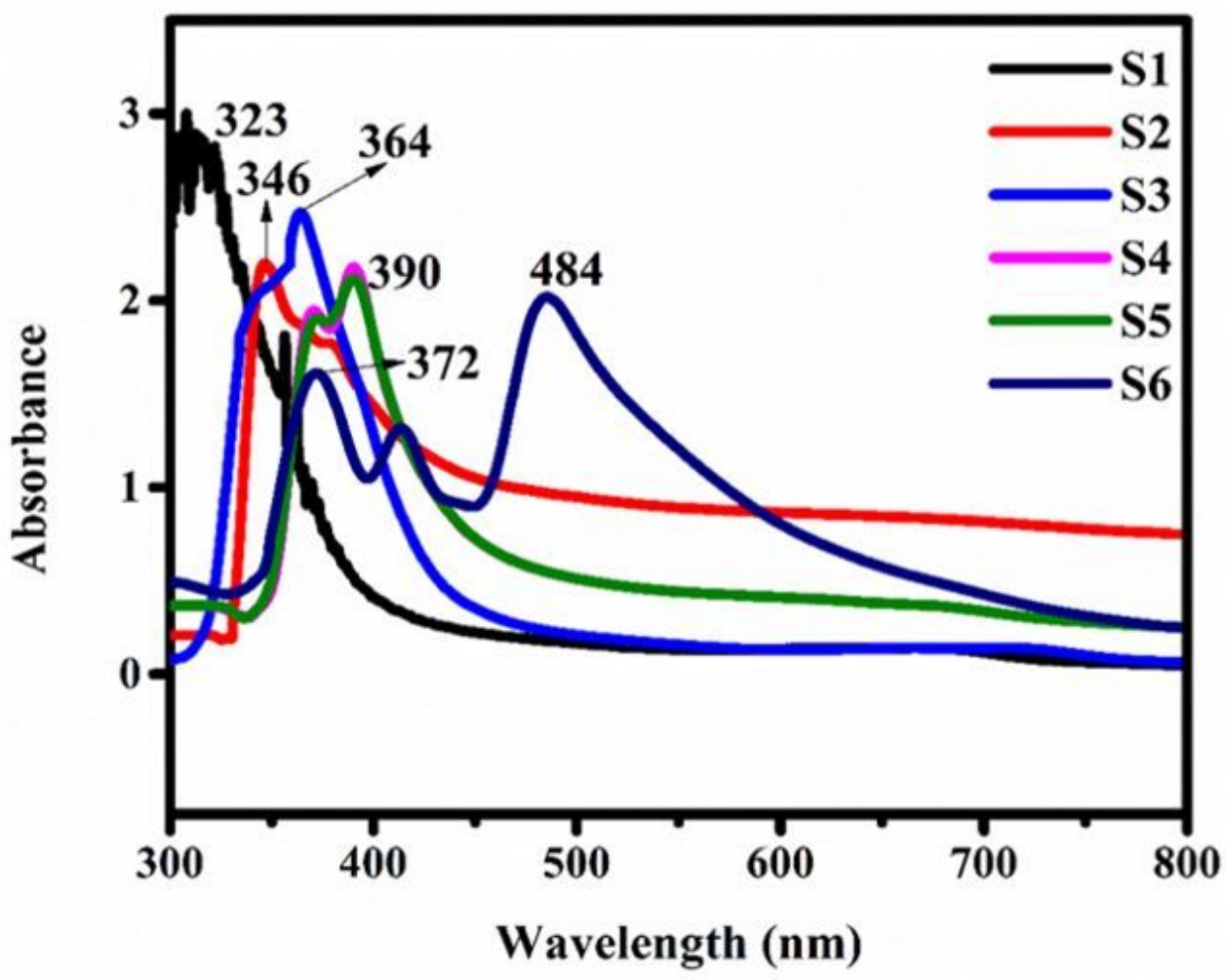

Figure 1

Ultraviolet-Visible spectrum of Nickel ferrite of samples S1 (Jr.NiFe2O4) and S2 to S6 annealed at different temperature.

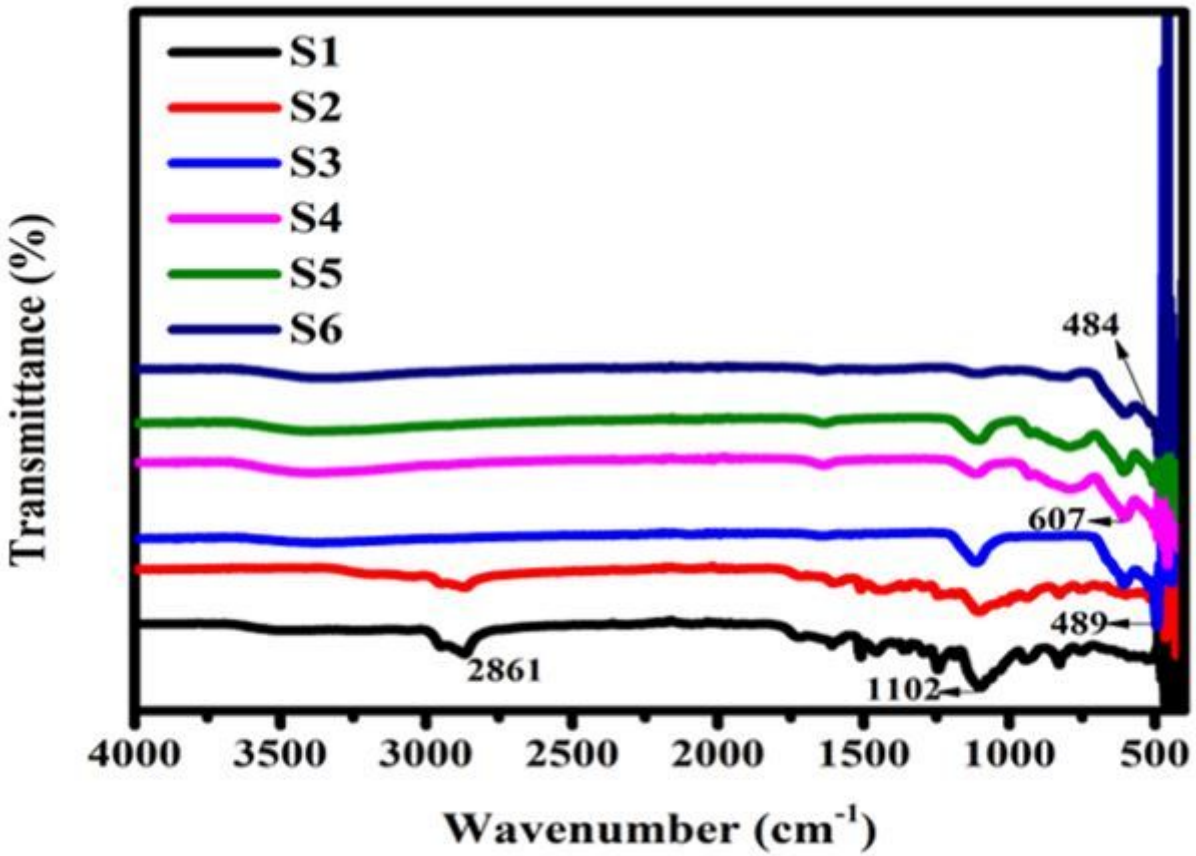

Figure 2

FTIR spectrum of nickel ferrite samples S1 (Jr.NiFe2O4) and S2 to S6 annealed at different temperature.

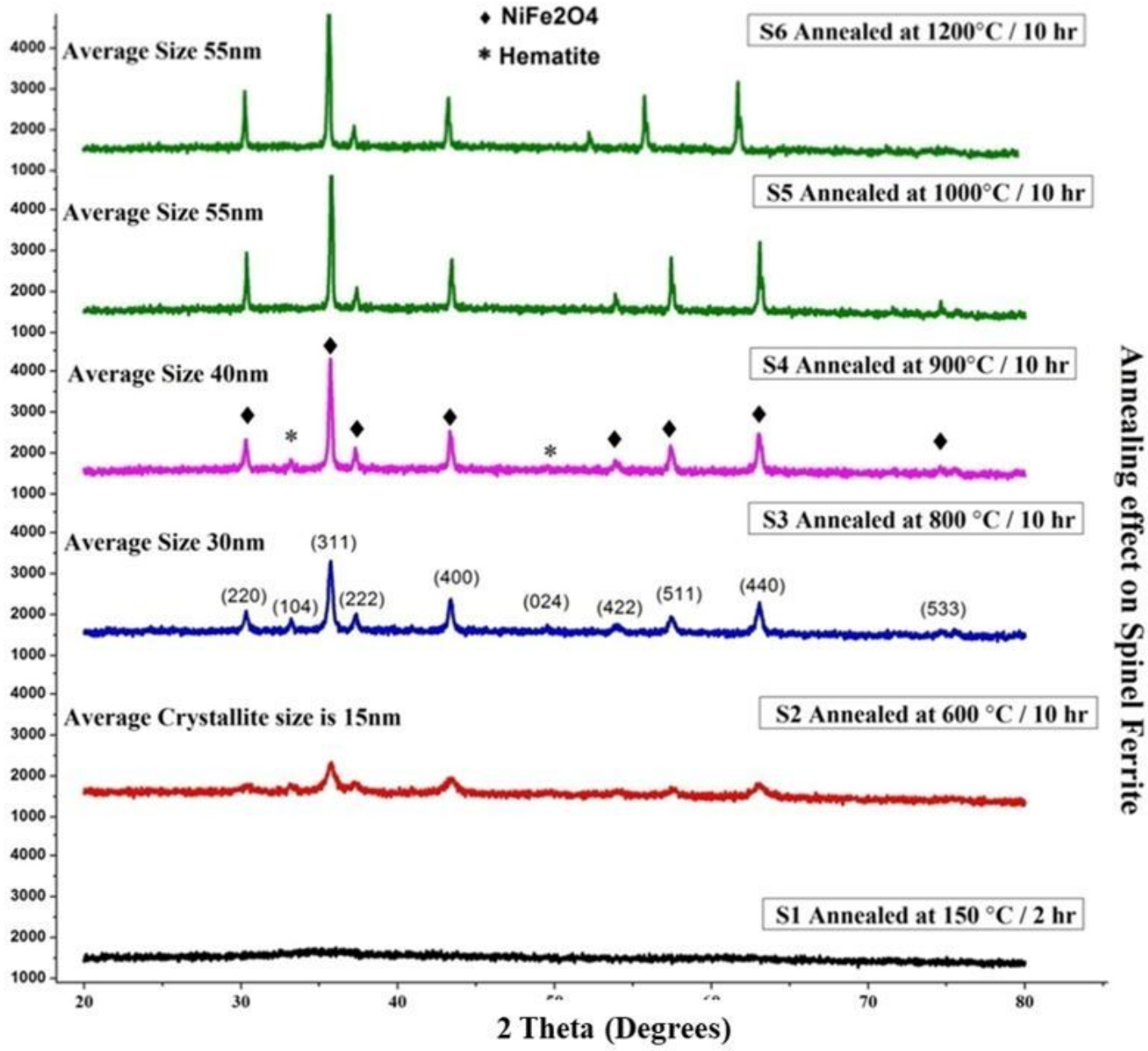

Figure 3

XRD patterns of samples (Jr.NiFe2O4) and S2 to S6 annealed at different temperature and for different periods

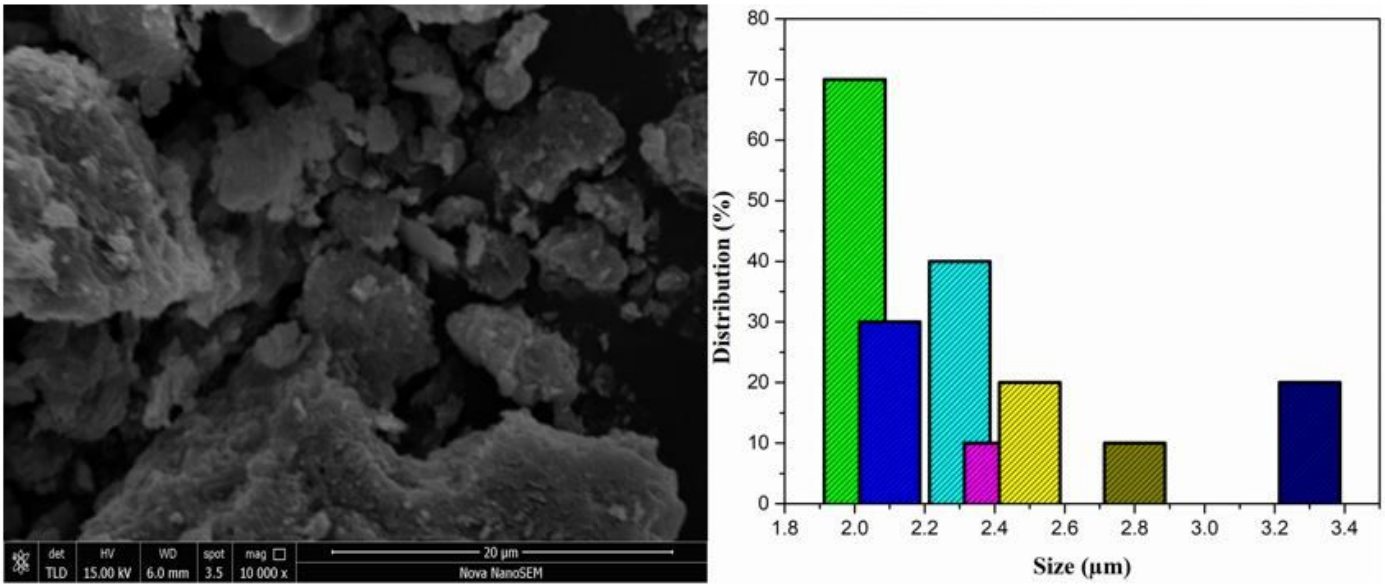

Figure 4

Scanning electron micrographs of Jr.NiFe2O4 Nps

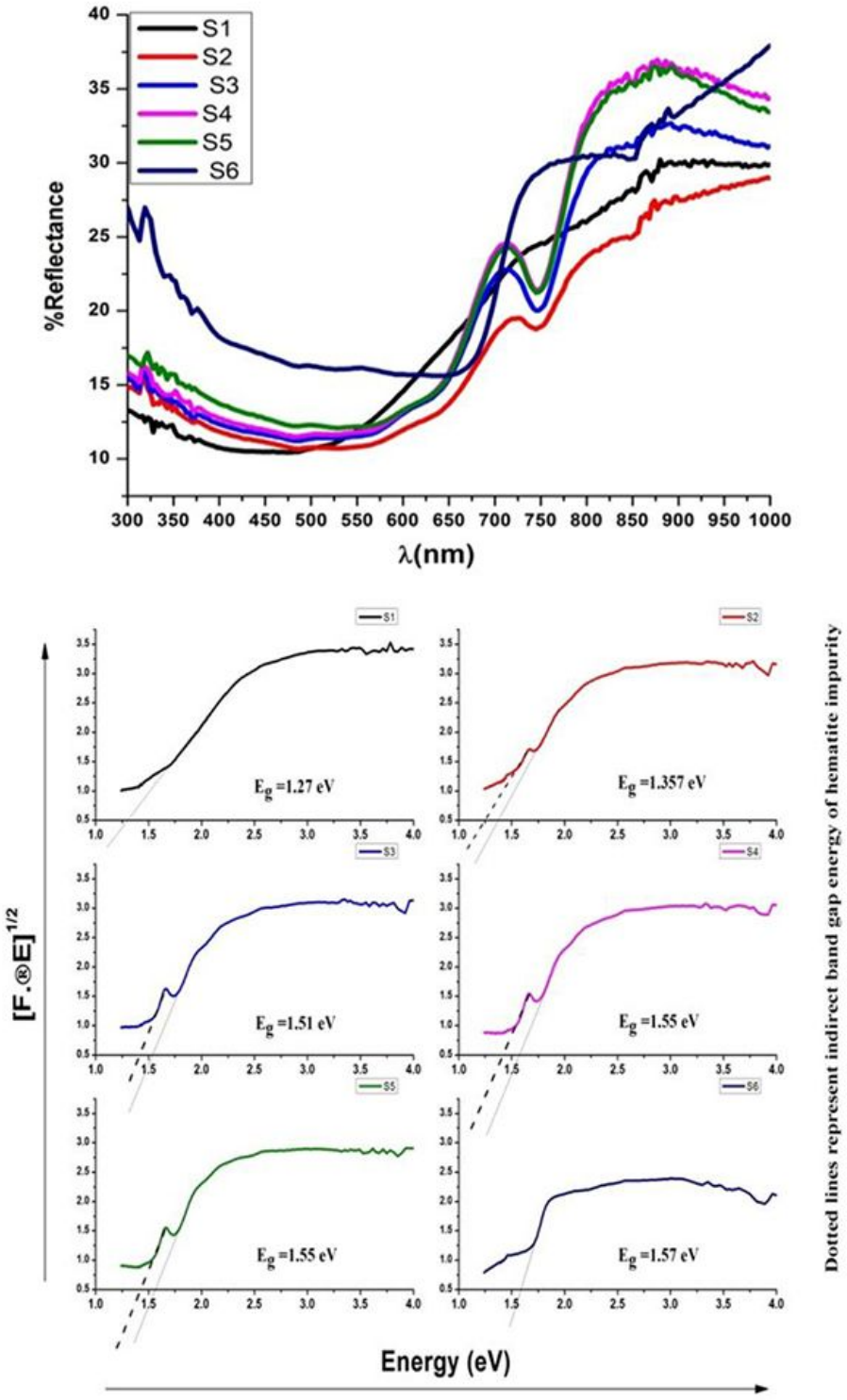

Figure 5

a Reflectance spectra of samples annealed at different b Reflectance spectra of Jr.NiFe2O4 samples annealed at different temperature

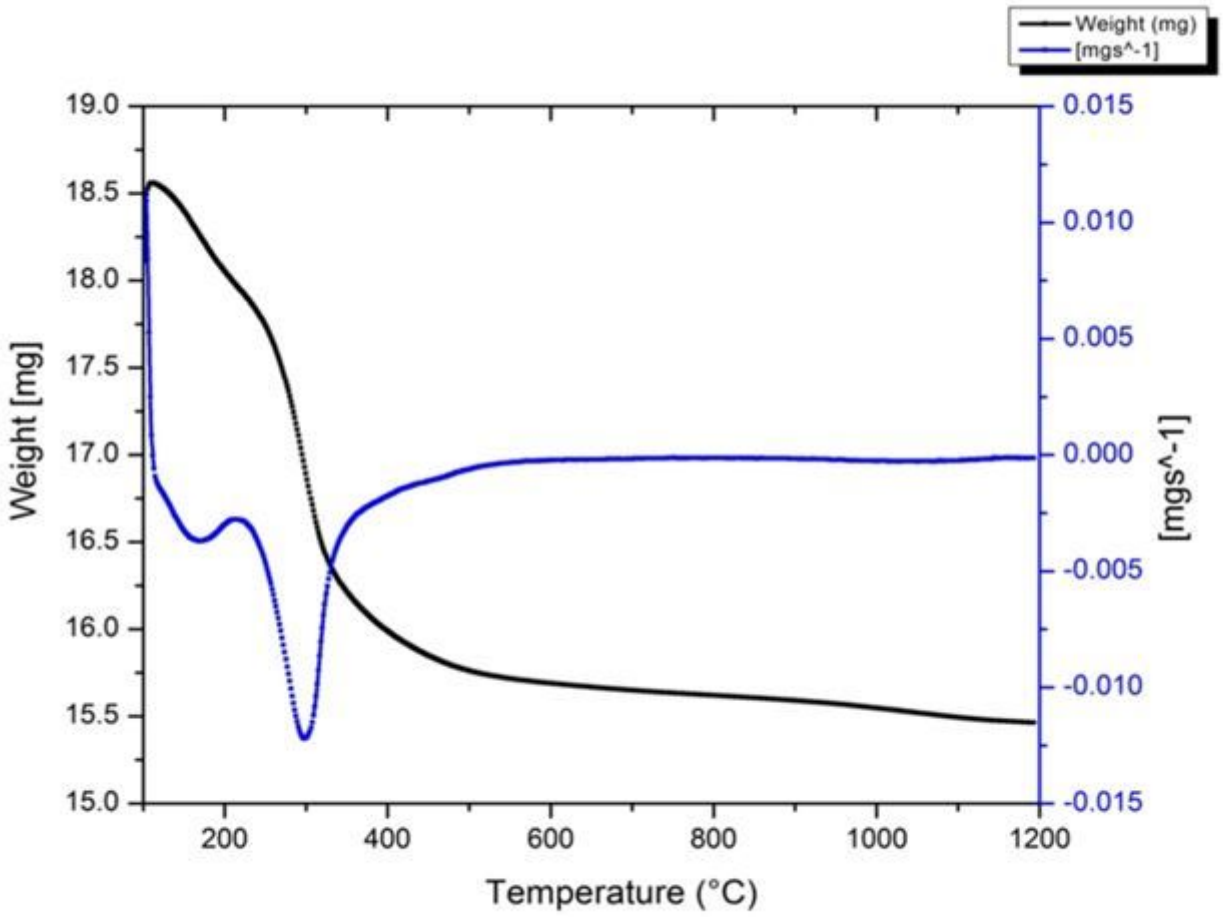

Figure 6

TGA/ DTA graph of Jr.NiFe2O4 Nps

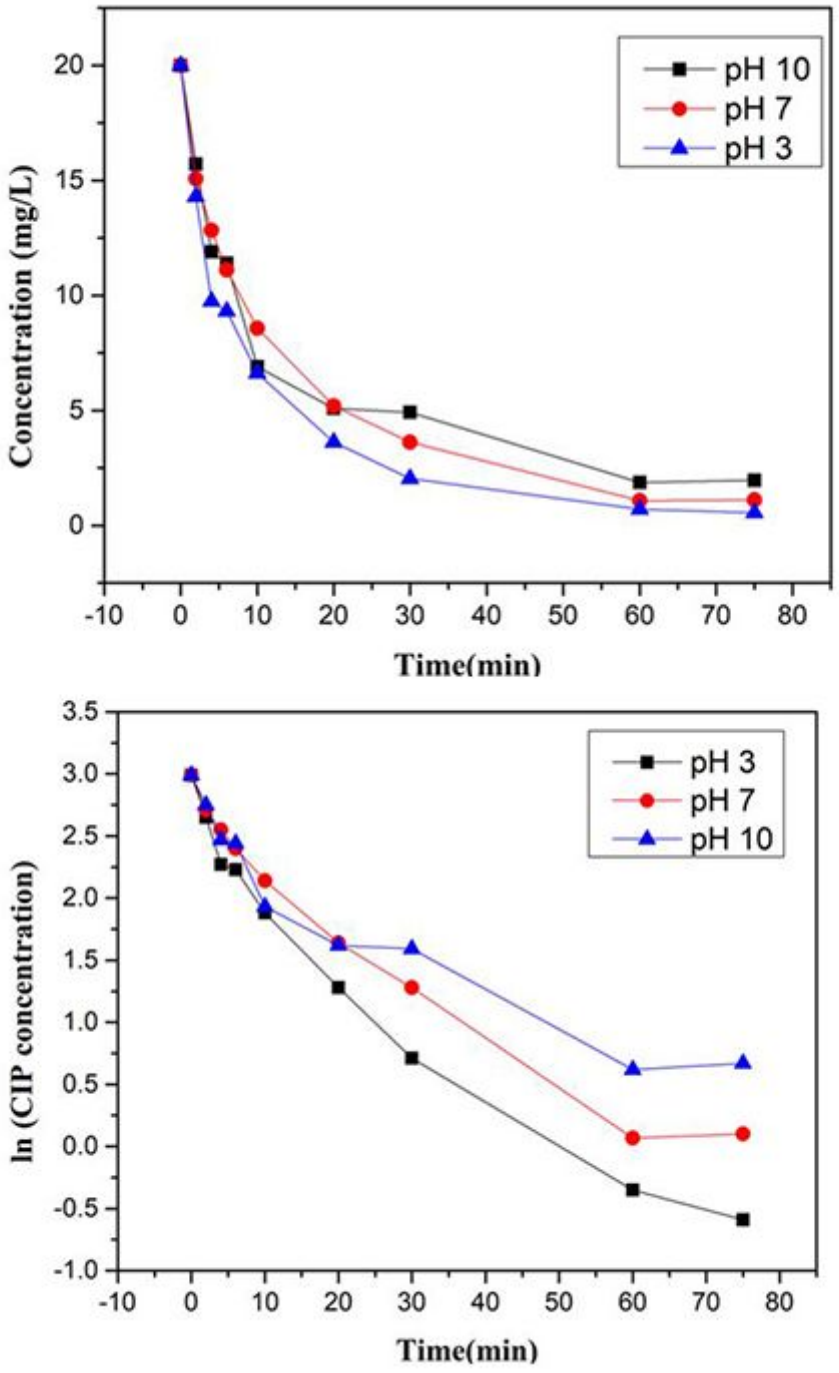

Figure 7

a Degrading potency of Jr.NiFe2O4 NPs (CIP conc. Verses time graph) b Degrading potency of Jr.NiFe2O4 NPs (ln CIP conc. vs time graph)

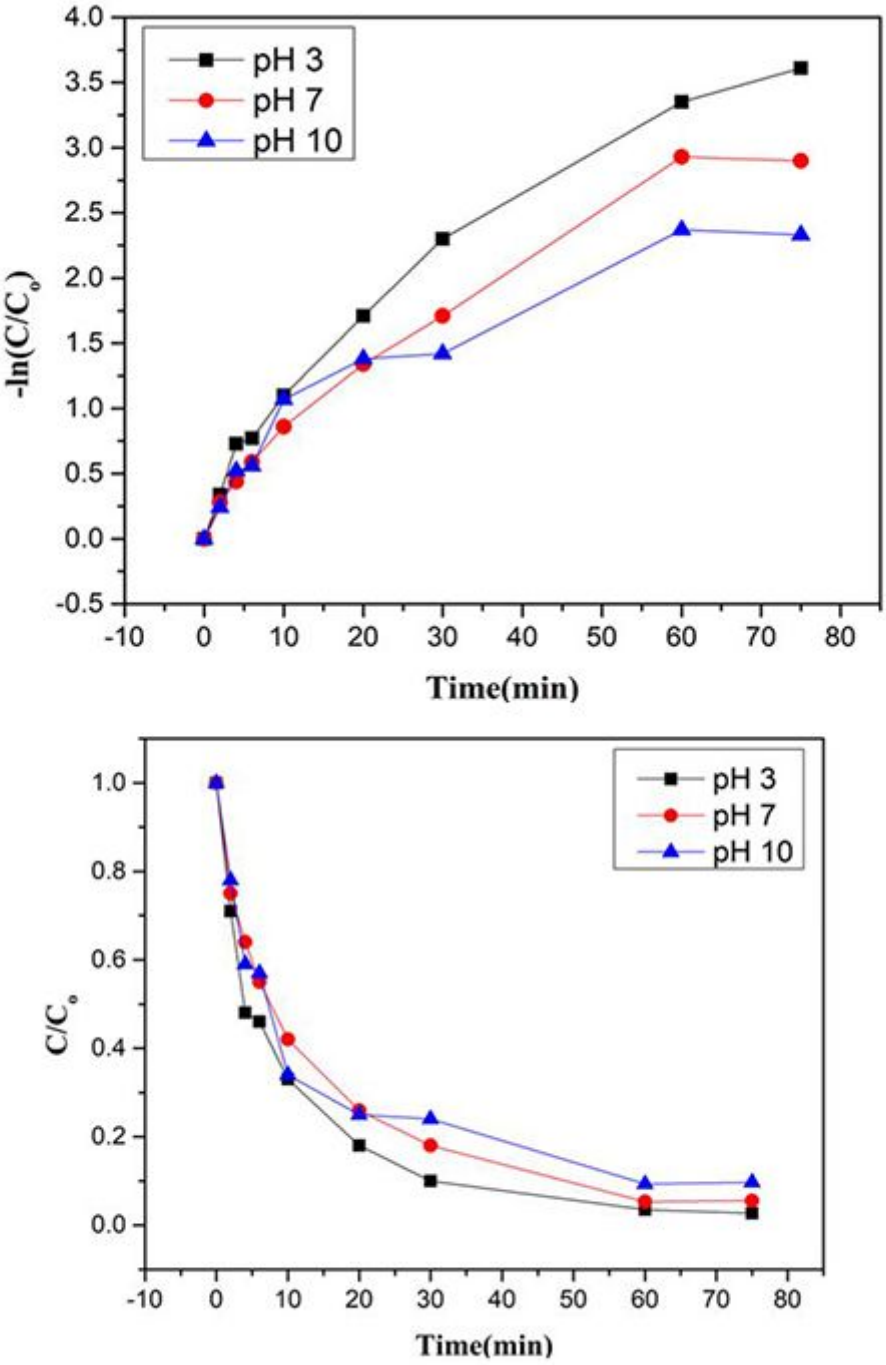

Figure 8

a Degrading potency of Jr.NiFe2O4 NPs (Kinetic plot of −ln(C/Co) vs time) b Degrading potency of Jr.NiFe2O4 NPs (Kinetic plot of C/Co vs time)

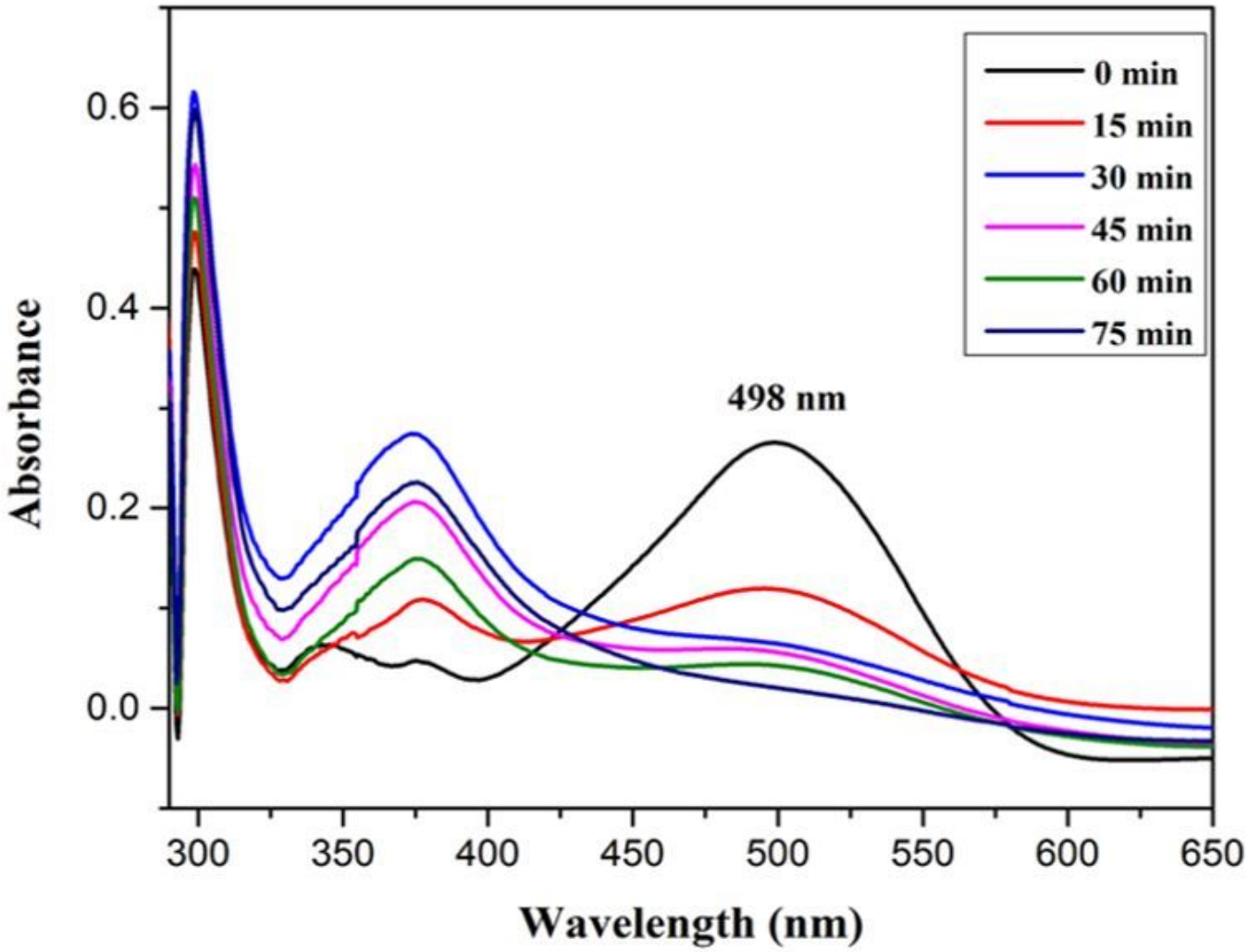

Figure 9

Absorption Spectra of CR dye at different time intervals

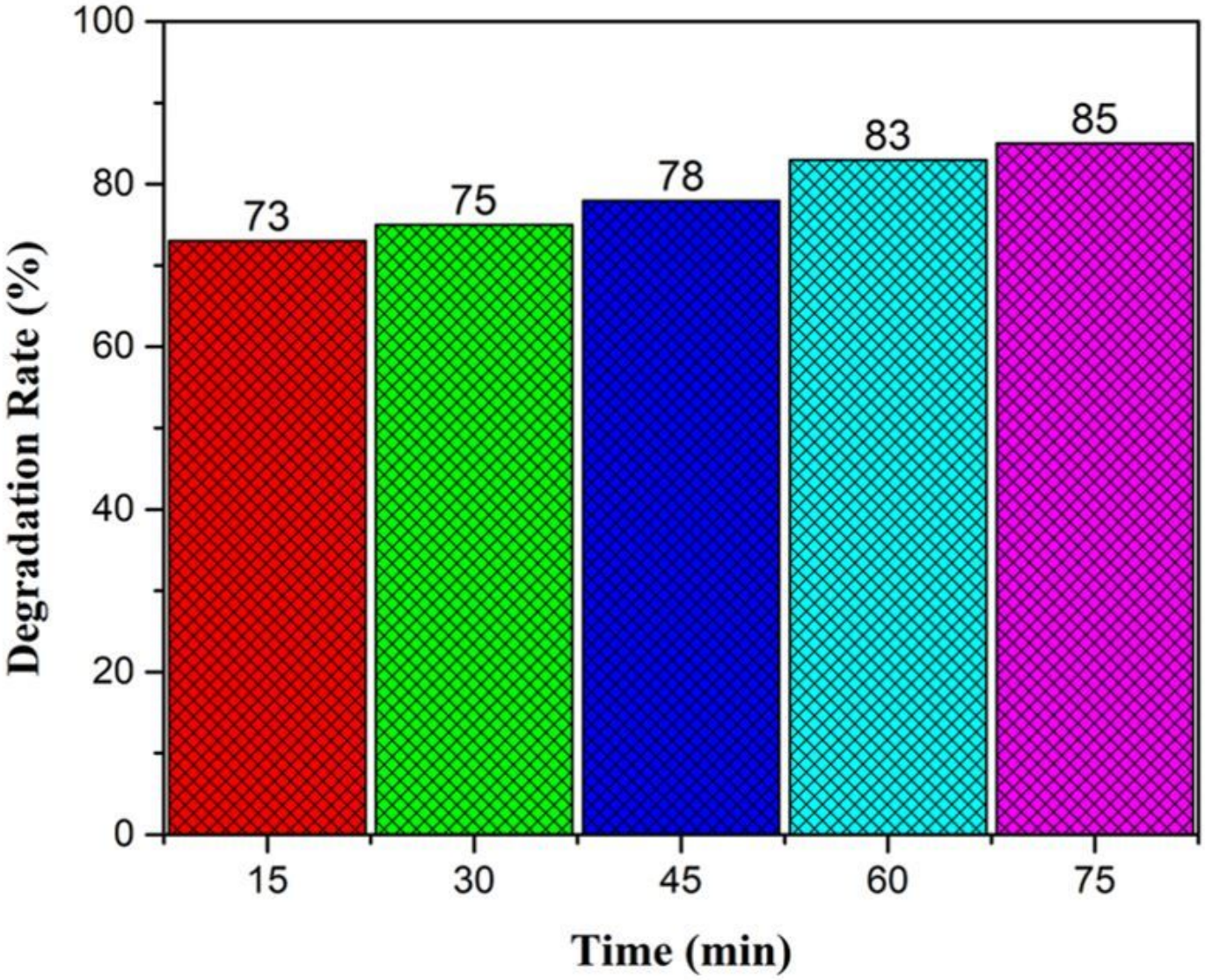

Figure 10

Degradation rate of CR under visible light irradiation

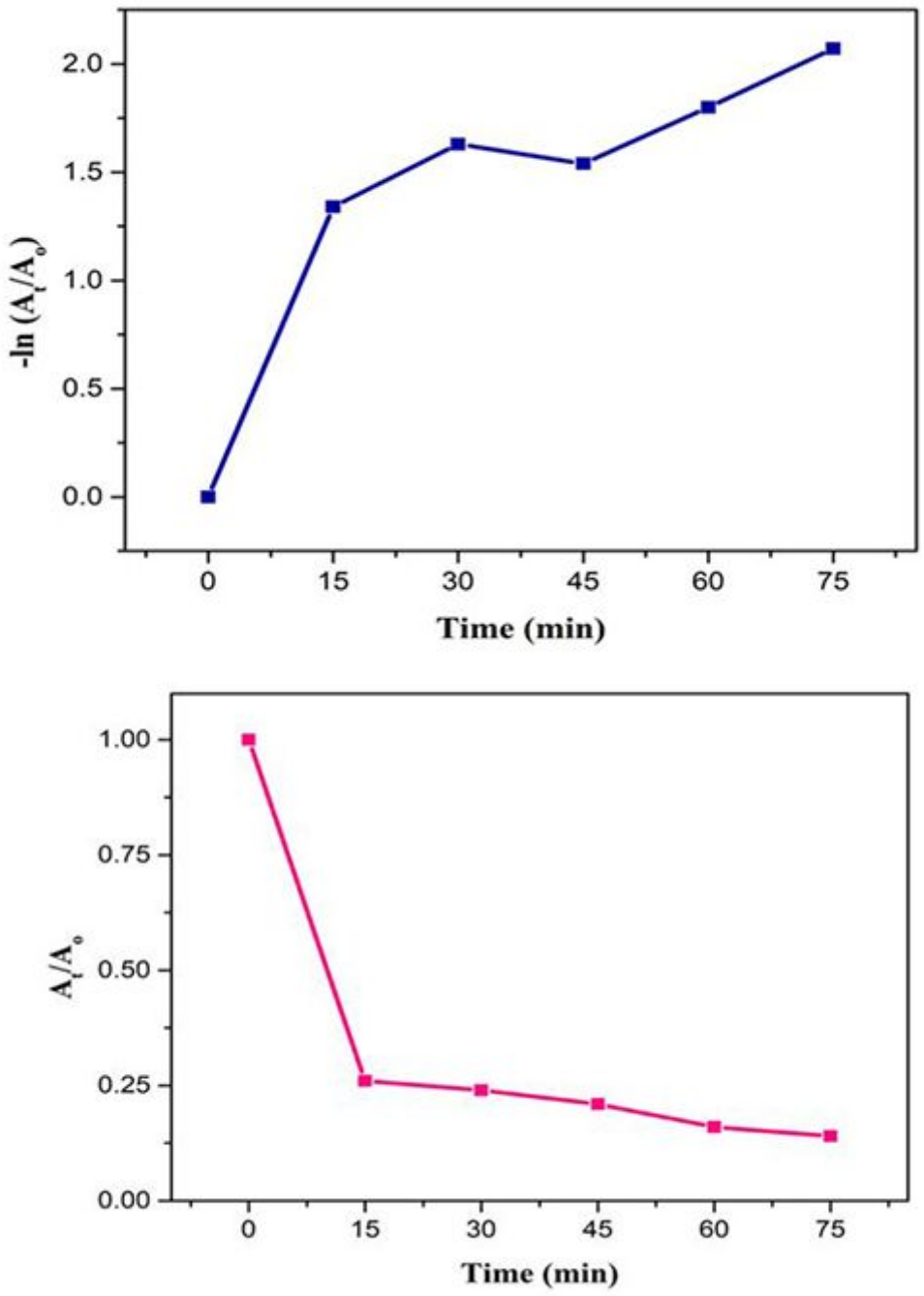

Figure 11

a Kinetic plot for degradation of CR, a plot of –ln(At/Ao) vs time b Kinetic plot of degradation of CR, a plot of At/Ao vs time

Supplementary Files

This is a list of supplementary files associated with this preprint. Click to download.

- Supplimentarymaterial.pdf